JACS
JOURNAL OF THE AMERICAN CHEMICAL SOCIETY
Article
pubs.acs.org/JACS

Concerted Growth and Ordering of Cobalt Nanorod Arrays as Revealed by Tandem in Situ SAXS-XAS Studies

Benoit Cormary,[†] Tao Li,[‡] Nikos Liakakos,[†] Laurent Peres,[†] Pier-Francesco Fazzini,[†] Thomas Blon,[†] Marc Respaud,[†] A. Jeremy Kropf,[§] Bruno Chaudret,[†] Jeffrey T. Miller,[§,∥] Elizabeth A. Mader,*[,§] and Katerina Soulantica*[,†]

[†]Université de Toulouse, INSA, UPS, LPCNO, CNRS-UMR5215, 135 avenue de Rangueil, 31077 Toulouse, France

[‡]X-ray Sciences Division and [§]Chemical Sciences and Engineering Division, Argonne National Laboratory, 9700 South Cass Avenue, Lemont, Illinois 60605, United States

[∥]School of Chemical Engineering, Purdue University, 480 Stadium Mall Drive, West Lafayette, Indiana 47097, United States

Supporting Information

ABSTRACT: The molecular and ensemble dynamics for the growth of hierarchical supercrystals of cobalt nanorods have been studied by in situ tandem X-ray absorption spectroscopy−small-angle X-ray scattering (XAS-SAXS). The supercrystals were obtained by reducing a Co(II) precursor under H_2 in the presence of a long-chain amine and a long-chain carboxylic acid. Complementary time-dependent ex situ TEM studies were also performed. The experimental data provide critical insights into the nanorod growth mechanism and unequivocal evidence for a concerted growth−organization process. Nanorod formation involves cobalt nucleation, a fast atom-by-atom anisotropic growth, and a slower oriented attachment process that continues well after cobalt reduction is complete. Smectic-like ordering of the nanorods appears very early in the process, as soon as nanoparticle elongation appears, and nanorod growth takes place inside organized superlattices, which can be regarded as mesocrystals.

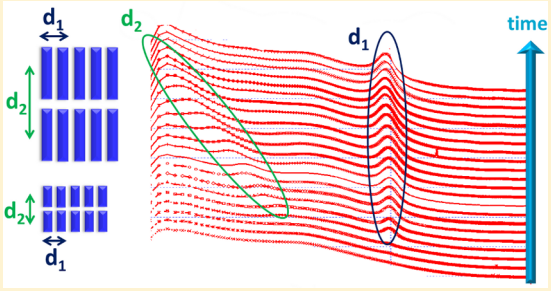

INTRODUCTION

Recent progress in the synthesis of size- and shape-controlled nanoparticles by colloidal chemistry[1,2] has been accompanied by a considerable effort to organize them into ordered superlattices and to understand the fundamental principles that lead to organization.[3−6] The synthesis of nanocrystal superlattices offers the opportunity to fabricate nanodevices composed of arrays of nanosized building blocks as well as to observe new collective properties stemming from interactions between their elementary units.[7,8] For example, single-crystalline cobalt nanorods are ideal candidates for applications in ultra-high-density magnetic recording devices due to their high magnetic moment and high magnetic anisotropy (magneto-crystalline and shape).[9] A regular array of Co nanorods positioned one next to the other and exposing their tips could correspond to a high-density magnetic recording configuration in which each nanorod would ideally represent a bit of information. Such arrays can be obtained during Co nanorod synthesis by H_2 reduction of organometallic or coordination Co compounds in the presence of long-chain amines and long-chain acids. The individual nanorods are single crystals of hexagonal close packed structure (*hcp*) and their long axis corresponds to the *c* axis of the *hcp* structure, that is, they grow along the [0001] crystallographic direction.[10,11] The direct formation of nanorod superlattices in solution involves both anisotropic growth and organization.

In general, two mechanisms by which size- and shape-controlled nanocrystal growth is achieved have been proposed. The first one involves nucleation and atom-by-atom attachment on less stable or imperfectly passivated facets of the already formed nuclei, followed by Ostwald ripening.[1,12,13] The second mechanism is based on oriented attachment of nanocrystals through which nanoparticles fuse together through high energy facets.[14−16] More recently in situ transmission electron microscopy (TEM) experiments have shown that both mechanisms are operational during the formation of Pt nanoparticles and PtFe nanorods.[17−19]

In parallel, organization of individual nanocrystals results in 2D or 3D single, binary, or ternary superlattices in which individual nanocrystals form regular networks.[20−22] Several techniques can be employed in order to organize nanoscale objects into regular arrays. Classical crystallization procedures are among the most popular, using the controlled evaporation of colloidal solutions of preformed nanoparticles as supercrystal building blocks.[23] Supercrystals formed by anisotropically shaped metal nanoparticles, among which nanorods,[24−30] are less common than the ones consisting only of spherical objects. Nevertheless, techniques for their organization are generally the same as for spherical nanoparticles. Thus, supercrystal synthesis

Received: February 21, 2016
Published: June 14, 2016

DOI: 10.1021/jacs.6b01929
J. Am. Chem. Soc. 2016, 138, 8422−8431

comprises several steps including building block synthesis, nanoparticle separation and purification, and assembly by an adequate technique, which is usually chosen by trial and error efforts.

Spontaneous nanocrystal organization in solution during growth giving rise directly to supercrystals that can be recovered after reaction has previously been described for some nanomaterials.[10,11,31−36] In some of these cases, the superlattices were characterized not only by translational but also by an impressive orientational order of the atomic lattices of individual nanocrystals within the assembly[32,33,36] and can be considered as mesocrystals.[37−39] Direct supercrystal growth involves two simultaneous processes, each one already complex and imperfectly understood. Generally, the superlattices are observed by TEM or scanning electron microscopy (SEM) on samples collected after reaction and, therefore, far away from the reaction conditions. Consequently, while the formation of the individual nanocrystals takes place during reaction, it is not known whether crystallization of the 3D supercrystals occurs during the nanomaterial synthesis or as an independent postgrowth step, for example, during cooling or drying on a microscopy grid. To better understand the direct synthesis of nanocrystal superlattices, it is important to determine the onset and evolution of nanocrystal growth and organization under reaction conditions. Recent in situ SAXS studies have shown supercrystal formation for Au nanospheres and nanowires in solution,[40,41] but to date, the 3D hierarchical organization of anisotropic nanocrystals has not been studied.

Herein, we study the formation of metallic Co nanorods and their simultaneous organization into 3D hierarchical assemblies using in situ X-ray absorption spectroscopy (XAS), small-angle X-ray scattering (SAXS), and ex situ TEM. We show that nanorods begin to form before reduction of the Co(II) precursor is complete and that they continue to grow well after Co(II) is fully reduced. We also demonstrate that formation and growth takes place in hierarchical 3D superstructures throughout the synthesis process.

EXPERIMENTAL SECTION

Materials. All solution preparations were performed in a glovebox due to the air sensitivity of the cobalt compounds. Anhydrous anisole packed under inert atmosphere was purchased from Aldrich (99.7%). Trace water was removed by activated molecular sieves. Hexadecylamine (HDA, 98%, Aldrich) and lauric acid (LA, 99%, Acros) were transferred in the glovebox and used without further purification. Toluene (99%, Fisher) was purified by a solvent purifier (Innovative Technology Purification System), degassed by three freeze−pump−thaw cycles, and then kept in the glovebox over activated molecular sieves. $[Co\{N(SiMe_3)_2\}_2(thf)]$[42] was purchased from NanoMeps. The synthesis of $[Co(LA)_2]$ was performed as previously reported.[43]

Synthesis of $[Co(LA)_2(HDA)_2]$. A solution of HDA (145 mg, 0.60 mmol in 4 mL toluene) is added to a solution of $Co(LA)_2$ (114 mg, 0.25 mmol in 2 mL toluene) under Ar and stirred overnight. When the stirring is stopped, a violet precipitate decants slowly from the colorless supernatant. The violet powder is isolated by filtration, washed twice with toluene and once with pentane, and then dried under vacuum. Yield 81%. Elemental Anal. C 71.48% (th. 71.5%), H 12.51% (th. 12.4%), N 3.01% (th. 2.98%).

Co Nanorod Synthesis. The nanorod stock solutions for XAS-SAXS measurements were prepared by mixing a solution of LA (49.7 mg, 0.25 mmol in 1 mL anisole) with a solution of HDA (84.4 mg, 0.35 mmol in 3.5 mL anisole). The mixture was stirred for 3 min. A solution of $[Co\{N(SiMe_3)_2\}_2(thf)]$ (94.1 mg, 0.21 mmol in 0.5 mL anisole) was rapidly added to the ligand mixture. After 5 min, 0.5 mL of the dark blue solution was transferred to a Meldin sample cup with a path length of 3.5 mm modified from Nelson and Miller.[44] The sample cup was sealed from air and moisture using a stainless-steel Swagelok VCO fitting modified with a pressure gauge, pressure relief valve (125 psi), and double ball valves to allow the addition of hydrogen under pressure. The sample was then removed from the glovebox, pressurized to 50 psi H_2, and placed in the thermally equilibrated sample holder described in the Supporting Information. The solution was not stirred during the reaction. When XAS-SAXS observations were complete, the sample cup was cooled and transferred into the glovebox where residual pressure was released.

TEM. TEM observations were performed in Toulouse using a JEOL JEM-1011 microscope equipped with a W thermionic electron source and working at an acceleration voltage of 100 kV or with a JEOL JEM 1400 microscope equipped with LaB6 thermionic electron source and working at an acceleration voltage of 120 kV. Postreaction samples were prepared by drop-casting from both the crude solution and a 0.1 mL aliquot of the crude solution diluted with 1 mL of toluene. For the size distributions, a minimum of 200 particles have been measured in all samples. High-resolution transmission electron microscopy (HRTEM) and selected area electron diffraction (SAED) images have been obtained using a JEOL 2100F electron microscope operated at 200 keV. A camera length of 20 cm has been used to obtain SAED patterns. All image analysis has been performed using Gatan Digital Micrograph.

SEM. SEM observations were performed on samples from crude solutions prepared as above on a JEOL JSM 6700F instrument.

Ex Situ Reaction Monitoring by TEM. To obtain TEM samples from the reaction products at different synthesis times, the stock solutions were mixed as above but scaled to double the amount of the starting solution and then divided into 1 mL aliquots which were introduced into 15 mL Fischer−Porter pressure vessels. The vessels were pressurized at 3 bar (43.5 psi) of H_2 and heated with stirring at 150 °C and without stirring at 130 °C in order to mimic in situ XAS-SAXS experiment conditions. The reaction was stopped at fixed time intervals by quenching in cold water before depressurizing and preparing the TEM grids as above. The slight differences in nanorod dimensions between the in situ XAS-SAXS and ex situ TEM experiments are expected due to the differences in the experimental setups.

Tandem X-ray Absorption Spectroscopy and Small-Angle Scattering. X-ray measurements were performed at the Advanced Photon Source, Argonne National Laboratory. The XAS and tandem XAS-SAXS measurements were collected on an insertion device beamline (Sector 10-ID), part of the Materials Research Collaborative Access Team (MR-CAT). SAXS-only measurements were collected on an insertion device beamline, (Sector 12-ID-B,C) part of the X-ray Sciences Division (XSD). Details of the experimental setup and analysis are provided in the Supporting Information.

RESULTS AND DISCUSSION

The reduction of $[Co\{N(SiMe_3)_2\}_2(thf)]$ (0.042M) in the presence of 1.2 equiv of LA and 1.7 equiv of HDA under 3 bar H_2 in anisole at 150 °C for 24 h yields metallic Co nanorods organized in 3D superlattices of a few micrometer lateral dimensions as evidenced by SEM and TEM (Figure 1). These hierarchical assemblies are composed of several superimposed 2D arrays of nanorods, organized side by side with their long axes perpendicular to the TEM grid in a smectic liquid crystal configuration. Spherical nanoparticles are also produced. The nanorods can be dispersed into single rods upon dilution with toluene, without reorganization into 3D superlattices upon drying.

Monitoring the nanorod growth by TEM (Figure S1) reveals that after 20 min the reaction yields both spherical Co nanoparticles (diameter: 3.3 ± 0.5 nm) and rods (diameter: 3.5 ± 0.5 nm) with an average length of ∼15 nm that are already aligned along their long axes. After 60 min, the length of the rods has increased; however, the size distribution is multimodal,

DOI: 10.1021/jacs.6b01929
J. Am. Chem. Soc. 2016, 138, 8422−8431

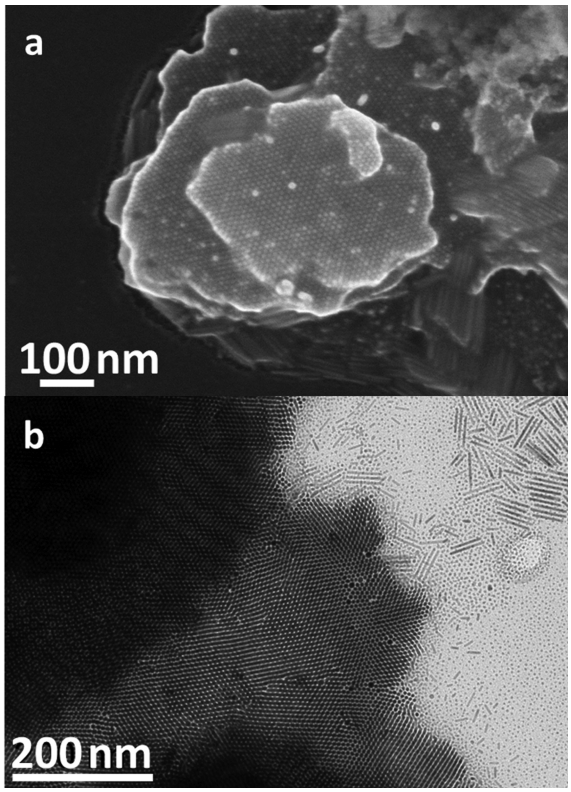

Figure 1. (a) SEM and (b) TEM micrographs of 3D superlattices obtained after 24 h reaction at 150 °C.

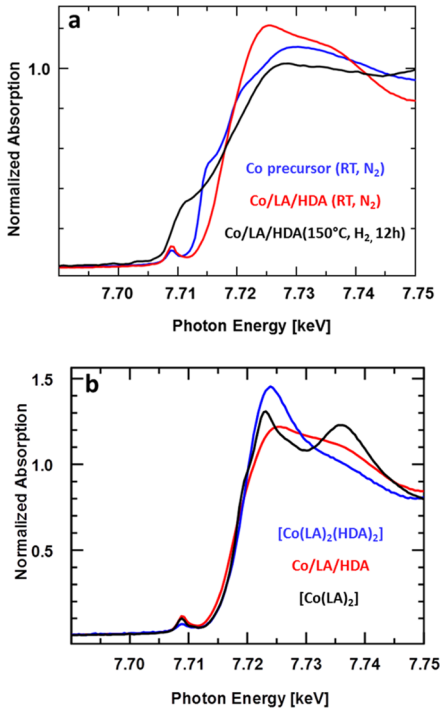

Figure 2. Co K-edge XANES spectra from 7690 to 7750 eV of (a) precursor $[Co\{N(SiMe_3)_2\}_2(thf)]$ at RT (blue); reaction mixture ($[Co\{N(SiMe_3)_2\}_2(thf)]$/LA/HDA = 1:1.2:1.7) under N_2 or H_2 at RT (red); reaction mixture under 50 psi H_2 after 12 h at 150 °C (black) and (b) $[Co(LA)_2]$ (black); $[Co(LA)_2(HDA)_2]$ (blue); reaction mixture ($[Co\{N(SiMe_3)_2\}_2(thf)]$/LA/HDA = 1:1.2:1.7) under N_2 at RT (red).

with the longer rods having already attained their final mean size. After 24 h, the size distribution of the rod length is again essentially monomodal (length: 57 ± 5 nm, diameter: 4.3 ± 0.7 nm), with the short rods having been converted to longer ones. Thus, the rods appear early in the synthesis, and their length evolves first rapidly and then more slowly, passing from a multimodal size distribution to a narrower size distribution after about 24 h. Spherical nanoparticles are always present, and their diameter remained practically unchanged over the course of the reaction (about 3.4 nm at the end of the reaction).

Initial Speciation of Co(II). Time-dependent in situ XAS was used to follow the evolution of both the oxidation state and coordination environment of a solution composition over the course of this reaction (Figure 2 and Table S1). The Co K-edge XANES of $[Co\{N(SiMe_3)_2\}_2(thf)]$ in anisole at room temperature (RT) shows a pre-edge feature at 7708.9 eV, characteristic of Co(II) (Figure 2a, blue spectrum).[45] The fit of the first shell peak in the EXAFS indicates there are an average of 2.8 Co−X (either Co−N or Co−O) bonds at 1.92 Å, typical for an average of two amide bonds at 1.87−1.91 Å[46−49] and a dative bond to thf at 2.1−2.2 Å.[50−52] EXAFS also shows evidence of a higher shell bond, likely from the overlap of Si and Me groups (Figure S2a).

Addition of $[Co\{N(SiMe_3)_2\}_2(thf)]$ to a 1.2:1.7 mixture of LA/HDA in anisole at RT maintains the XANES pre-edge peak at 7709.0 eV (Figure 2a, red spectrum), indicating that the cobalt remains Co(II). The change in the shape of the XANES, however, indicates a change in the ligand coordination of the Co(II) ion. Quantitation of the EXAFS indicates that on average there are 6 Co−N/O bonds at a distance of 2.02 Å (Figure S2b). Because EXAFS is a bulk technique and the scattering from Co−N is very similar to that of Co−O, this likely represents the average of several Co(II) species and ligand coordination environments.

To better understand the possible Co(II) species present in the initial synthesis solution, the XAS spectra of $[Co(LA)_2]$ and $[Co(LA)_2(HDA)_2]$ were measured (Figure 2b). Both have XANES pre-edge peaks consistent with Co(II). $[Co(LA)_2]$ has a white line region with two bands of approximately equal intensity at 7723.1 and 7736.0 eV. EXAFS fitting gives 6 Co−O bonds at 1.98 Å, suggesting that this species is oligomeric with carboxylate ligands bridging between multiple cobalt centers.[53] $[Co(LA)_2(HDA)_2]$ has only one white line peak, and the fit of the EXAFS gives 6 Co ligand (Co−O and/or Co−N) bonds at 2.08 Å. Both the XANES and EXAFS indicate that there is a change in the Co coordination sphere on addition of HDA to $[Co(LA)_2]$. The XANES and EXAFS of the initial Co nanorod synthesis solution and $[Co(LA)_2(HDA)_2]$ are very similar suggesting that the reactive Co(II) species are also similar. Consistent with this, $[Co(LA)_2]$ is stable toward reduction by H_2 for at least 14 h, whereas complete Co(II) reduction occurs in the presence of free amine.[43] Therefore, we propose that in the starting solution $[Co\{N(SiMe_3)_2\}_2(thf)]$ rapidly exchanges ligands to a mixture of LA and HDA coordinated species, the exact composition of which is dependent on the LA/HDA ratio and changes during the reaction.

Reduction of Co(II) to Co(0). The composition of the initial mixture is not affected by the addition of 50 psi (3.4 bar) H_2 at RT. However, upon heating to 150 °C under H_2, changes in the XANES and EXAFS spectra indicate the reduction of Co(II) to metallic Co (Figure 2a, black spectrum). The absorption edge energy and shape at the end of the reaction are identical to that of a metallic foil (Co(0)). The XANES spectra

DOI: 10.1021/jacs.6b01929
J. Am. Chem. Soc. 2016, 138, 8422−8431

were fitted with a linear combination of the initial reaction mixture and the fully reduced Co at the end of the 12 h reaction. A plot of the molecular fraction of Co(II) versus time (Figure S3a), shows an initial first-order reduction of Co(II) species, followed by a more rapid reduction after about 17−20 min, where about 70% of the Co(II) has been reduced. Co(II) is completely reduced to metallic Co in less than about 30 min, after which there are no further changes in the XANES (or EXAFS) up to 12 h. A fit of the EXAFS gives a Co−Co coordination number of 7.6 and a bond distance of 2.49 Å. The distance is characteristic of Co metal, and the reduced average coordination number (foil CN = 12) corresponds to a particle size of ∼3−4 nm in diameter assuming a spherical shape.[54] TEM observation of the undiluted sample after the 12 h XAS experiment shows the presence of nanorod superlattices (Figure S3b). Independent ex situ TEM experiments (described above) indicate that the nanorod length continues to evolve up to about 24 h (Figure S1). It has to be noted that Co reduction to Co(0) molecular or cluster compounds that are not immediately nucleated is not evidenced from the XAS data, which is in agreement with the ex situ TEM, indicating that nucleation of the first nanocrystals is very fast. Variations in the experimental conditions (pressure, the reactor volumes H_2 pressure, and mixing; see Experimental Section) complicates direct comparison between laboratory and in situ XAS synthesis; however, the dramatic difference in time scales between Co(II) reduction and rod growth as well as the fact that no size defocusing is observable even after all monomer is depleted[12,13] suggests that a nonclassical growth mechanism is involved in the nanorod formation.[16,38,55]

To better follow the reduction of Co(II) and the formation of the 3D superlattices, the reaction temperature was reduced to 130 °C for tandem in situ XAS-SAXS experiments. The same reaction mixture of $[Co\{N(SiMe_3)_2\}_2(thf)]$/LA/HDA was reacted at 130 °C and 50 psi H_2 for approximately 3 h. Figure 3a shows selected XANES spectra during the reaction. The initial XANES of the reaction mixture (Figure 3a, red spectrum) was identical to that at 150 °C. The XANES were fit with a linear combination of the initial reaction solution and the reduced metallic Co after 3 h. Figure 3b shows the log of the percent of Co(II) reduced to Co(0) versus time. After an initial induction period of 25 min where there is no reduction of Co(II), a slow, approximately first-order reduction of Co(II) to metallic Co begins. At 70 min (∼54% Co(II) remaining), the rate of Co reduction starts to increase and continues until 80−90 min, when only 25% Co(II) is left.

After 105 min at 130 °C, there is no further change in the XAS. The fully reduced particles display a XANES spectrum that is essentially the same as bulk Co foil. The EXAFS spectrum (Figure 3c) shows Co−Co bonds with an average coordination number of 8.9 at 2.51 Å, consistent with metallic Co of about 4−5 nm in diameter. Similar to the results at 150 °C, the XAS Co−Co coordination is the same at 100 min and 3 h. TEM on the final reaction mixture shows both nanorod superlattices and spherical nanoparticles (Figure 3d; dimensions in Figure S4). Thus, the Co nano-object size obtained by EXAFS is an average between the spherical nanoparticle diameter and the rod diameter. The increasing rate of Co(II) reduction observed at both 130 and 150 °C suggests that reduction may be autocatalytic, where the final Co(II) species are reduced by the already formed cobalt nanoparticles,[56] or alternatively, as the reduction proceeds, more easily reduced Co(II) species are formed by free amine liberated during Co

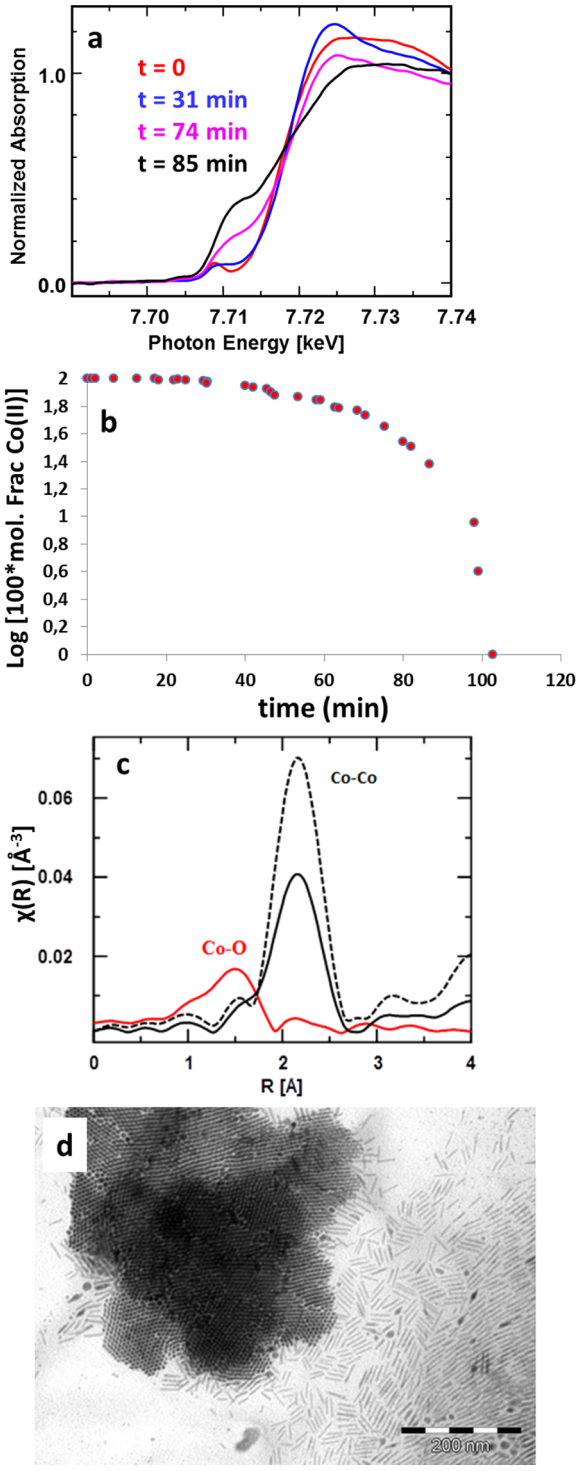

Figure 3. (a) Time-dependent XAS spectra during the synthesis of Co nanorods at 130 °C and 50 psi H_2 ($[Co\{N(SiMe_3)_2\}_2(thf)]$/LA/HDA = 1:1.2:1.7). Co K-edge XANES from 7.69 to 7.74 keV. Initial spectrum (red), at 31 min (blue), at 74 min (pink) and at 85 min (black). (b) Log[%Co(II)] vs time determined by XANES fitting. (c) Co K-edge k^2-weighted magnitude of the Fourier transform of the EXAFS of the starting reaction mixture at 130 °C (red trace), Co nanorods after reaction at 130 °C (black solid trace), and Co foil at RT (black dotted trace) (Δk = 2.9−10.7 $Å^{-1}$). (d) TEM micrograph of a superlattice obtained from the crude reaction after 3h at 130 °C (scale bar =200 nm).

DOI: 10.1021/jacs.6b01929
J. Am. Chem. Soc. 2016, 138, 8422−8431

nanoparticle formation. This is supported by previous studies showing that while $Co(LA)_2$ alone cannot be reduced by H_2 at 150 °C, addition of amine induces its reduction.[43]

Nano-Object Formation and Organization by SAXS. SAXS provides information about the size, distribution, shape, and organization of nano-objects in solution.[57−60] Figure 4a,b

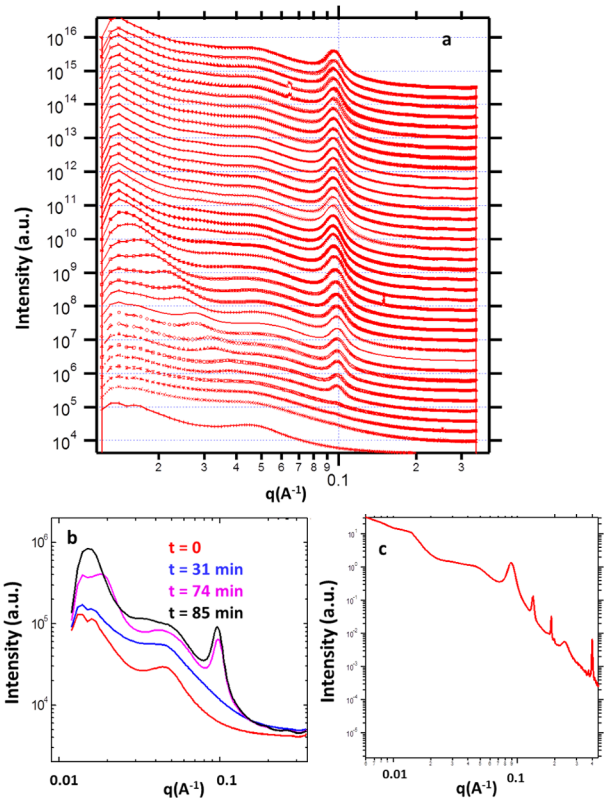

Figure 4. (a) In situ SAXS part of the time-dependent spectra of tandem SAXS-XAS experiment for the formation of Co-nanorods at 130 °C and 50 psi H_2 SAXS at 8979 eV. (b) Selected time points from a. Initial spectrum (red) and those at 31 min (blue), 74 min (pink), and 85 min (black). (c). Ex situ SAXS of the sample after reaction at quartz capillary at energy of 12 keV with a camera distance of 2 m.

show the time-dependent in situ SAXS spectra concurrently recorded with the XAS measurements at 130 °C. A broad peak at q = 0.047 Å^{-1} remains unchanged over the course of reaction and is attributed to the Meldin sample holder. At 35 min, a broad peak appears at q_1 = 0.099 Å^{-1}, indicating the formation of organized nano-objects. The intensity of q_1 increases over the reaction (Figures 4a and 5a), corresponding to an increase in the number of organized nano-objects. At about 40 min, a second peak clearly appears at a lower q (q_2 = 0.038 Å^{-1}) whose intensity similarly increases with reaction time. Over the course of reaction, q_1 shifts only slightly, whereas q_2 continuously shifts to lower q and thus longer distance (Figure 5b).

We interpret q_1 and q_2 as organized lamellar arrays of hexagonally packed nanorods with a small lateral rod−rod distance that during the reaction increases from 7.4 to 7.6 nm ($d_1 = (4\pi/\sqrt{3})q_1$).[59,61] Interestingly, the slight increase in the inter-rod distance takes place during the reduction acceleration interval (70−90 min) observed by XAS. The smaller nanorod diameter measured by TEM compared to d_1 suggests that the inter-rod volume is occupied by molecular species and solvent.[57,58] This is also consistent with the difference between

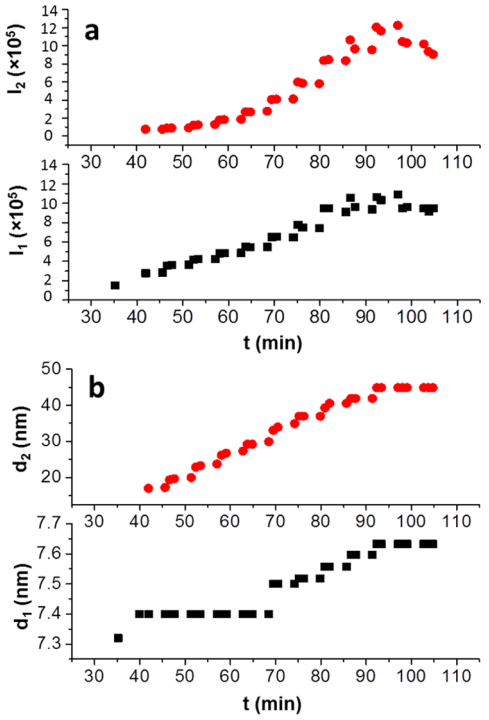

Figure 5. (a) Peak intensity of time-dependent SAXS peaks (I_1: q_1 = 0.099 Å^{-1}, I_2: q_2 = 0.038 Å^{-1}) and (b) d-spacing of center to center (d_1) (in plane distance) and rod to rod length (d_2) (interlamellar distance) during the synthesis of Co nanorod superlattices at 130 °C and 50 psi H_2.

the internanorod distance (7.5 ± 0.8 nm) and the nanorod diameter (4.9 ± 0.7 nm), evidenced by TEM after the end of the reaction (3 h, Figure S4).

An interlamellar spacing of 16.5 nm ($d_2 = 2\pi/q_2$)[59] starts to be visible at 40 min and smoothly increases to 45 nm after 90 min (Figure 5b). After about 90 min, we can no longer follow elongation due to the limitation of the q range accessible in this experiment. Nevertheless, the in situ SAXS conclusively demonstrates that superlattice organization occurs under the synthesis conditions.

The SAXS features associated with lamellar arrays overlap with the broad peak from our sample holder, and the q range of the detector was limited. Thus, after reaction, RT ex situ SAXS measurements over a wider q range (0.006−0.45 Å^{-1}) were obtained in a quartz capillary tube (Figure 4c). The rod−rod distance is observed at q = 0.090 Å^{-1}. Three broad peaks at q = 0.014, 0.028, and 0.042 Å^{-1} correspond to the lamellar structure, and the d spacing is calculated to be 45 nm, i.e., the same as the in situ SAXS and longer than the nanorod length measured by TEM (37.5 nm) after the end of the reaction (Figure S4). Finally, there are four sharp peaks at q = 0.134, 0.188, 0.198, and 0.4 Å^{-1} associated with a body-center-cubic (bcc) packing of spherical nanoparticles with an interparticle distance of 5.7 nm. Again, this is larger than the dry TEM diameter of 3.6 ± 0.5 nm for the spherical nanoparticles, consistent with expansion of the lattice due to molecular compounds (surfactants and solvent; Figure S4).

Comparison with ex Situ TEM. Time-dependent TEM studies under similar reaction conditions at 130 °C in the laboratory provide information complementary to the tandem in situ XAS-SAXS data (Figure S5). Reaction mixtures quenched at 15 min contain mainly spherical nanoparticles of

DOI: 10.1021/jacs.6b01929
J. Am. Chem. Soc. 2016, 138, 8422−8431

2.5 ± 0.5 nm and some wormlike nano-objects. The latter become predominant at 25 min (Figure S6). At 30 min, short nanorods with a well-defined elongated shape have already formed organized arrays with an average length of 10 nm. At 40 min, the nanorods have begun to lengthen and grow to about 25 nm, and a larger percentage are found in organized superlattices. At 60 min the length distribution becomes bimodal, with most rods still around 25 nm and a smaller fraction of longer ones averaging 35 nm and growing to 55 nm at 3 h. At 27 h, the majority of the nanorods have reached a mean length of 55 nm (Figure S5).

Ex situ TEM and in situ SAXS results are in general agreement about the sequence events and kinetics of superlattice formation. Both results suggest that nanorod organization begins at the same time as nanoparticle elongation, very early in the synthesis. In addition, the nanorods continue to lengthen with time but do not significantly increase in diameter. As in the case of 150 °C, TEM shows that at 130 °C nanorod length continues long after all the Co(II) has been fully reduced to metallic Co, the nanorod diameter is slightly increased during the reaction, and spherical nanoparticles are always present.

Mesocrystal Character of the Superlattices. The characteristic mesocrystal crystallographic register of the individual nanorods within the 3D organized superlattices has been evidenced by TEM on samples obtained after different reaction times, as can be seen from Figure 6. The nanorod positional order is obvious both from the TEM images and the fast Fourier transform (FFT) of the areas included in the yellow squares. The common crystallographic orientation of the individual nanocrystals is evidenced by the selected area electron diffraction (SAED) performed on the areas in the cyan circles. Presented in Figure S7, the HRTEM analysis on a superlattice nanorod allows us to identify the lateral Co surfaces as the {11−20} *hcp* facets. A schematic representation of the organization of the nanorods within the superlattice is also shown (Figure S7).

Evolution of Co Nanorod Superlattice Formation. In Scheme 1 we outline in a simplified way the complex events leading to the formation of superlattices.

Reduction Step. Altogether our results suggest that for both reaction temperatures the Co reservoir is rapidly reduced; however, this reduction is characterized by two regimes. The first step, which is preceded by an induction period, is followed by a more rapid step. We believe that the first step corresponds to the nucleation and the formation of the first spherical nanoparticles from easily reduced amine-rich species present in the Co reservoir[43] and their aggregation to ill-shaped nano-objects (step 1 in Scheme 1). During nucleation, the labile amines (HDA and $HN(SiMe_3)_2$) are the main ligands available for the nanoparticle stabilization because the LA initially is mostly coordinated to the Co(II) slowly reducible species.[43] Thus, the initially formed nuclei can aggregate forming the ill-shaped nano-objects observed by ex situ TEM at 15 min reaction and 25 min at 130 °C (Figure S6). However, subsequent reduction of Co(II) laurate-rich species liberates LA ligands that can now interact with the surface of the spherical or ill-shaped nanoparticles initially formed. Initial nuclei may be subjected to dissolution−precipitation process before crystallizing to seeds from which anisotropic growth can initiate. Previous studies have shown that an increase of the LA amount in solution increases the *hcp* versus the *fcc* (face-centered cubic) component in the produced nano-objects and favors anisotropic growth.[43] Under the present conditions, as the laurate-rich species start to be reduced, the availability of laurate ligand induces the crystallization of the *hcp* structure. This is the onset of the anisotropic growth and the formation of

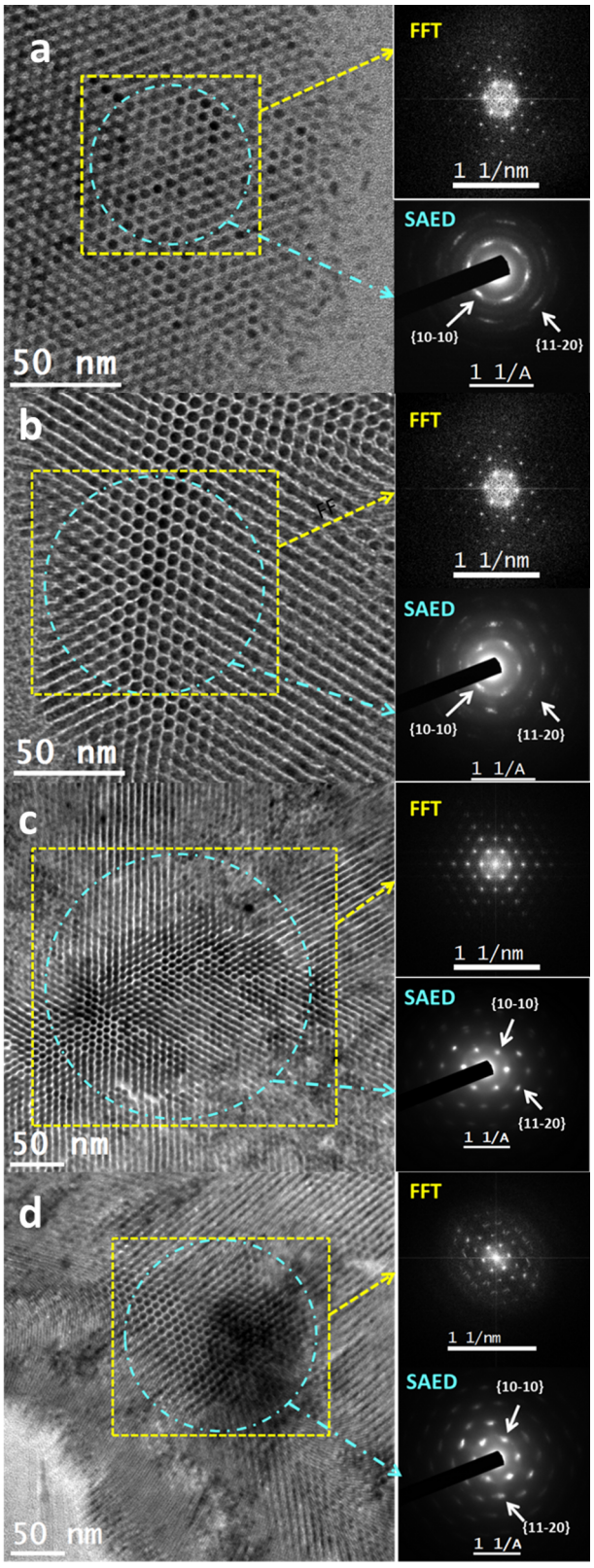

Figure 6. TEM images FFT and SAED patterns of the regions indicated with yellow squares and cyan circles respectively, for different reaction times: (a) 40 min, (b) 1 h, (c) 3 h, and (d) 24 h.

DOI: 10.1021/jacs.6b01929
J. Am. Chem. Soc. 2016, 138, 8422−8431

Scheme 1. Proposed Reaction Pathway

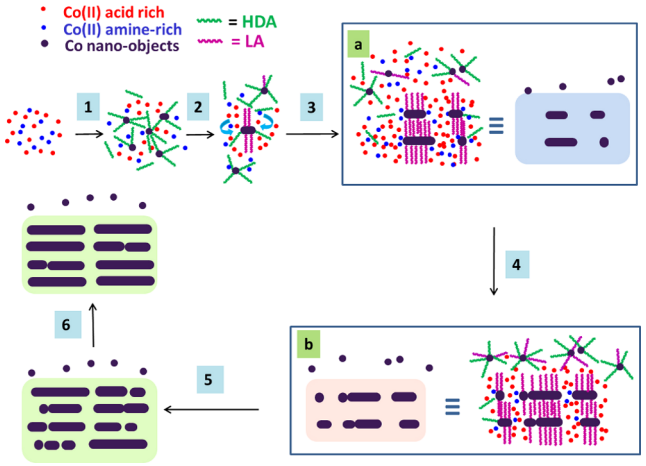

well-shaped nanorods (step 2 in Scheme 1). We presume that during subsequent Co(II) reduction nanorod growth takes place principally by preferential monomer addition on the nanorod tips that are less efficiently passivated, probably mainly by labile amine ligands (step 3 in Scheme 1). At the same time, Co atoms are marginally incorporated along the lateral sides that we believe are well-passivated by laurate. During the second fast reduction step, less-reactive carboxylate-rich species are rapidly reduced due to the assisted reduction by free amine available in solution. This conversion of stable acid-rich species to easily reducible amine-rich species probably induces also the formation of new nuclei during the whole reduction period. An autocatalytic effect of the Co nanocrystal surface is probably also taking place and could be responsible for the fast growth of the nanorods in length during that time.[56] Thus, as long as Co(II) is present in the solution medium, Co atom addition on the nanorods is proposed to be the main reaction path. The size distribution during initial anisotropic growth does not point toward an oriented attachment because no dimers or trimers of spherical nanoparticles are identified. Nevertheless, although not evident due to the atom-by-atom growth being simultaneous and dominant, oriented attachment is most probably also operating during this stage. Growth of spherical nanoparticles as well as rods both by monomer addition and by oriented attachment of spherical nanoparticles operating in parallel has been already observed through real-time TEM studies on growing spherical[17,18] or rod-shaped metallic nanoparticles.[19] This process is represented by steps 3−5 in Scheme 1.

Elongation Step. One question that arises is whether the final slow elongation step taking place after Co reduction continues via an atom-by-atom growth followed by Ostwald ripening or via oriented attachment (nanosphere−nanosphere, rod−rod, or rod−nanosphere). In our case, anisotropic growth is favored both by the inherently anisotropic *hcp* structure, as well as by the inefficient passivation of the Co(0002) facets by the labile amine ligands versus the efficient passivation of the lateral facets by the laurate ligand. Both characteristics may allow deposition of Co atoms on as well as fusion of nano-objects through the "naked" Co(0002) facets. Oriented attachment usually gives rise to structural defects and irregular surfaces. It has to be noted that the nanorods are single-crystalline and that their aspect is smooth with a homogeneous diameter along the entire length pointing toward an atom-by-atom Ostwald ripening classical growth mechanism. However, once the monomer concentration is reduced, if Ostwald ripening was the dominating ripening mechanism, then size defocusing would lead to less monodispersed size distributions,[12,13] which is not in agreement with the experimental data that show that the diameter is practically stable and that length distribution is narrowed with time. Thus, oriented attachment is likely to be dominant in this slow growth step. However, a contribution of Ostwald ripening after Co(II) reduction could explain surface smoothness because atom diffusion to metal deficient sites operating simultaneously could eliminate defects and repair surface irregularities.[19] Thus, we suggest that, for the slow growth regime taking place after Co(II) consumption, oriented attachment is the main process by which elongation takes place (steps 5−6 of Scheme 1). To summarize, taking into account the reduction kinetics and the nanoparticle lengthening evolution, we believe that both classical and nonclassical processes take place: during reduction, atom-by-atom growth is dominant, whereas oriented attachment is dominant during the slow elongation observed after reduction has been completed.

Organization. Rationalizing organization even when starting from preformed nanocrystal building blocks, for which the surface chemistry is more or less controlled, is not straightforward. A delicate balance between attractive and repulsive interparticle interactions (van der Waals, electrostatic, steric, entropic effect, hydrogen bonding, etc.) are responsible to varying degrees depending on the nanocrystal composition and shape, the surfactants, and the solvents used. In the case of direct organization during growth, things are even more complicated because the solution composition and therefore the interaction possibilities change with time. It has already been reported in the literature that an amide can be formed by condensation of long-chain amines with long-chain acids are heated together.[62] Amide is not a strong ligand and can be easily displaced by acid from incoming precursors. This could not only induce depletion attractions between the nano-objects[63] but also influence the interactions between molecular species or nano-objetcs through formation of hydrogen bonds in which water resulting from the condensation reaction could also participate. The presence of magnetic dipolar forces may assist the oriented attachment of nano-objects, but we do not believe that it is the unique driving force for the hierarchical organization because addition of toluene dissolves the supercrystals irreversibly. It must also be noted that the same type of spontaneous organization has been observed during non-magnetic nanoparticle growth.[32,36,40]

TEM indicates that superlattices are observed as soon as shape anisotropy appears (situation denoted a in Scheme 1), that is, before Co(II) reduction is finished, and they continue to grow well after the reduction is over. We cannot exclude the possibility that 2D organization is the first step of supercrystal nucleation because the center-to-center lateral distance appears before lamellar order is visible. However, the presence of the Meldin cell signal does not allow us to be affirmative about this point. What is worth noting without any doubt is that the rods grow in length while organized, and length polydispersity does not seem to be detrimental for the 3D organization (Figure S8). Thus, growth happens inside the 3D architecture which remains loosely held together as indicated by the in situ and ex situ SAXS measurements, suggesting that the final interlamellar distances do not correspond to the real nanorod length even if we take into account the presence of long-chain ligands on the

DOI: 10.1021/jacs.6b01929
J. Am. Chem. Soc. 2016, 138, 8422−8431

tips (37.5 nm for the longer nanorods measured by TEM and 45 nm by ex situ SAXS after 3 h reaction; Figure S4). We have proposed that both atom-by-atom as well as oriented attachment mechanisms operate during growth. This suggests that monomers diffuse easily through the organized 2D layers that constitute the 3D supercrystals. The molecular Co reservoir that is fed by the bulk solution and changes composition as the reaction proceeds could gradually crystallize within the confined interlayer space (Scheme 1a,b). In contrast, an efficient oriented attachment implies that nanocrystals are free to translate and rotate before crystallographic alignment and fusion is achieved.[39,64] This mechanism would be difficult to operate in the context of a growth inside a confined space where spatial restrictions prevent the free movement of the nano-objects unless an appropriate prealignment of nano-objects and/or Co monomers occurs in that space represented by the shaded areas of Scheme 1 rendering a rotation of nano-objetcs unnecessary before fusion along the long nanorod axis.

Recently, a lamellar organometallic phase was detected in solution giving rise to ultrathin Au nanowires, and it has been proposed that this mesophase could be responsible for anisotropic growth.[65] An environment-dependent growth mode has also been proposed to be responsible for the formation of Fe nanocubes superlattices in which supramolecular organization controls the nanocrystal shape.[35] In this study, we have no evidence that a preorganization of the liquid medium acts as a template for superlattice formation. Although micelles have been detected in the starting solution at RT, at the elevated temperatures at which our reaction takes place, there was no SAXS evidence of an organized mesophase. However, we can speculate that a structuring of the reaction medium in which superlattices grow is not pre-existent but takes place as the reaction proceeds, for instance, by liberation of amide and water as a result of a condensation reaction. These areas of continuously evolving composition (symbolized by different colors of the shaded areas in Scheme 1) and distinct composition from the bulk solution could allow monomer circulation and nanorod growth both by monomer addition and oriented attachment.

Spherical Nanoparticles. Concerning the fate of spherical nanoparticles, our experimental SAXS set up prevents volume fraction monitoring, but extended reaction times at 130 and 150 °C (96 h) do not eliminate the spherical nanoparticles as shown by TEM (Figure S9). The persistence of spherical nanoparticles, even after extended reaction times, could be explained by the combined effect of (i) the nucleation being operational during the whole reduction period due to the amine activation of the acid-rich species, (ii) the medium structuring and partial confinement of the areas inside which nanorods grow, which after a certain time does not favor the incorporation of newly formed nano-objects from the bulk solution, and (iii) the freezing of the reactivity of these spherical nanoparticles due to the formation of a dense ligand shell as a result of the increase in concentration of carboxylic acid in the solution.

Thus, anisotropic interactions between passivated nano-objects but also molecular compounds could act synergistically to direct a concerted growth−organization pathway as in the case of mesocrystals.[37−39,66−71] It is likely that the already reported examples of some of the superlattices reported to be formed directly in solution are produced by a concerted growth−organization process and constitute similar cases. It has been invoked[36] that polar ligand systems inducing electrostatic interactions could promote the spontaneous formation of supercrystals during growth. This is a point that merits further investigation. Unfortunately, very few examples of the kind have been reported so far. In addition, the processes being simultaneous complicates a detailed study and rationalization of the process. We believe that the use of a combination of recently developed or future in situ observation capabilities by different techniques, along with theoretical studies, will greatly contribute to the elucidation of the development of such complex systems toward the rapid and one-pot synthesis of nanocrystal superlattices.

CONCLUSIONS

In situ tandem XAS-SAXS experiments supported by ex situ TEM monitoring of the reaction allow proposal of a qualitative nanorod growth mechanism, which consists of three main steps: a fast nucleation, a fast growth by monomer addition that takes place during reduction of Co(II) species to Co(0), and a slower ripening step that takes place after complete reduction, which most likely involves an oriented attachment process. Our results constitute definitive evidence that the growth of the individual nanorods and their organization in 3D smectic-like superlattices occur simultaneously under synthesis conditions and not as a result of postsynthesis crystallization of the nanorods. It is, thus, likely that nanorods grow in a confined reaction environment, allowing monomer diffusion and at the same time facilitating oriented attachment by assuring a favorable orientation of the nano-objects during their formation without compromising their organization. Although the main driving force for such a regular array formation is not straightforward, this concerted growth and organization process shares common features with mesocrystal formation. We finally believe that a deeper understanding of the ensemble dynamic processes taking place during this complex reactions in terms of molecular composition and nanomaterial evolution will allow one-pot synthesis of supercrystals to be extended to many systems.

ASSOCIATED CONTENT

Supporting Information

The Supporting Information is available free of charge on the ACS Publications website at DOI: 10.1021/jacs.6b01929.

Experimental setup for tandem XAS-SAXS; XAS data analysis; cobalt K-edge XANES and EXAFS in situ Fitting Results; monitoring of nanorod growth at 150 °C by ex situ TEM; table with the cobalt K-edge XANES and EXAFS in situ fitting results; Fourier transform of the EXAFS of $[Co\{N(SiMe_3)_2\}_2(thf)]$ and of the starting $[Co\{N(SiMe_3)_2\}_2(thf)]$/LA/HDA solution; evolution of the reduction at 150 °C by XANES and TEM of the final result; size distributions from TEM, after the tandem XAS-SAXS experiment at 130 °C; monitoring of nanorod growth at 130 °C by ex situ TEM; TEM of the nanoparticles obtained after 15 and 25 min at 130 °C; SEM of a superlattice of short nanorods; nanorod HRTEM; spherical nanoparticle persistence at different reaction times at 150 and 130 °C (PDF)

AUTHOR INFORMATION

Corresponding Authors

*E-mail: elizabeth.mader@yale.edu.

*E-mail: ksoulant@insa-toulouse.fr.

DOI: 10.1021/jacs.6b01929
J. Am. Chem. Soc. 2016, 138, 8422−8431

Present Addresses

N. L.: Chemical Sciences Division, Lawrence Berkeley National Laboratory, 1 Cyclotron Road, Berkeley, CA 94720, USA.
E.M.: Department of Chemistry, Yale University, PO Box 208107, New Haven, CT, 06520−8107, USA.

Notes

The authors declare no competing financial interest.

■ ACKNOWLEDGMENTS

B.C., N.L., B.C., and K.S. thank the ANR for the project BATMAG (ANR-07-BLAN-0296), the European Commission for the FP7 NAMDIATREAM project (EU NMP4-LA-2010-246479), the European Commission and the Région Midi-Pyrénées for the POCTEFA Interreg project (MET-NANO EFA 17/08). E.A.M. and A.J.K. acknowledge financial support from the Chemical Sciences and Engineering Division at Argonne National Laboratory. J.T.M. and T.L. were supported as part of the Institute for Atom-efficient Chemical Transformations (IACT), an Energy Frontier Research Center funded by the U.S. DOE, Office of Science, Office of Basic Energy Sciences. Use of the Advanced Photon Source (APS) is supported by the U.S. Department of Energy, Office of Science, Office of Basic Energy Sciences, under Contract DE-AC02-06CH11357. MRCAT operations are supported by the Department of Energy and the MRCAT member institutions.

■ REFERENCES

(1) Yin, Y.; Alivisatos, A. P. *Nature* **2005**, *437*, 664−670.
(2) Xia, Y.; Xiong, Y.; Lim, B.; Skrabalak, S. E. *Angew. Chem., Int. Ed.* **2009**, *48*, 60−103.
(3) Min, Y.; Akbulut, M.; Kristiansen, K.; Golan, Y.; Israelachvili, J. *Nat. Mater.* **2008**, *7*, 527−538.
(4) Bishop, K. J. M.; Wilmer, C. E.; Soh, S.; Grzybowski, B. A. *Small* **2009**, *5*, 1600−1630.
(5) Goubet, N.; Richardi, J.; Albouy, P.-A.; Pileni, M.-P. *Adv. Funct. Mater.* **2011**, *21*, 2693−2704.
(6) Frenkel, D. *Nat. Mater.* **2014**, *14*, 9−12.
(7) Nie, Z.; Petukhova, A.; Kumacheva, E. *Nat. Nanotechnol.* **2010**, *5*, 15−25.
(8) Talapin, D. V.; Lee, J.-S.; Kovalenko, M. V.; Shevchenko, E. V. *Chem. Rev.* **2010**, *110*, 389−458.
(9) Soulantica, K.; Wetz, F.; Maynadié, J.; Falqui, A.; Tan, R. P.; Blon, T.; Chaudret, B.; Respaud, M. *Appl. Phys. Lett.* **2009**, *95*, 152504.
(10) Dumestre, F.; Chaudret, B.; Amiens, C.; Respaud, M.; Fejes, P.; Renaud, P.; Zurcher, P. *Angew. Chem., Int. Ed.* **2003**, *42*, 5213−5216.
(11) Wetz, F.; Soulantica, K.; Respaud, M.; Falqui, A.; Chaudret, B. *Mater. Sci. Eng., C* **2007**, *27*, 1162−1166.
(12) Peng, X.; Manna, L.; Yang, W.; Wickham, J.; Scher, E.; Kadavanich, A.; Alivisatos, A. P. *Nature* **2000**, *404*, 59−61.
(13) Peng, Z. A.; Peng, X. *J. Am. Chem. Soc.* **2001**, *123*, 1389−1395.
(14) Banfield, J. F.; Welch, S. A.; Zhang, H.; Ebert, T. T.; Penn, R. L. *Science* **2000**, *289*, 751−754.
(15) Cho, K.-S.; Talapin, D. V.; Gaschler, W.; Murray, C. B. *J. Am. Chem. Soc.* **2005**, *127*, 7140−7147.
(16) Zhang, J.; Huang, F.; Lin, Z. *Nanoscale* **2010**, *2*, 18−34.
(17) Zheng, H.; Smith, R. K.; Jun, Y.; Kisielowski, C.; Dahmen, U.; Alivisatos, A. P. *Science* **2009**, *324*, 1309−1312.
(18) Yuk, J. M.; Park, J.; Ercius, P.; Kim, K.; Hellebusch, D. J.; Crommie, M. F.; Lee, J. Y.; Zettl, A.; Alivisatos, A. P. *Science* **2012**, *336*, 61−64.
(19) Liao, H.-G.; Cui, L.; Whitelam, S.; Zheng, H. *Science* **2012**, *336*, 1011−1014.
(20) Sun, S.; Murray, C. B.; Weller, D.; Folks, L.; Moser, A. *Science* **2000**, *287*, 1989−1992.
(21) Shevchenko, E.; Talapin, D. V.; Kotov, N. A.; O'Brien, S.; Murray, C. B. *Nature* **2006**, *439*, 55−59.
(22) Evers, W. H.; Friedrich, H.; Filion, L.; Dijkstra, M.; Vanmaekelbergh, D. *Angew. Chem., Int. Ed.* **2009**, *48*, 9655−9657.
(23) Liao, C.-W.; Lin, Y.-S.; Chanda, K.; Song, Y.-F.; Huang, M. H. *J. Am. Chem. Soc.* **2013**, *135*, 2684−2693.
(24) Young, K. L.; Personick, M. L.; Engel, M.; Damasceno, P. F.; Barnaby, S. N.; Bleher, R.; Li, T.; Glotzer, S. C.; Lee, B.; Mirkin, C. A. *Angew. Chem., Int. Ed.* **2013**, *52*, 13980−13984.
(25) Zhang, S.-Y.; Regulacio, M. D.; Han, M.-Y. *Chem. Soc. Rev.* **2014**, *43*, 2301−2323.
(26) Li, L.-S.; Walda, J.; Manna, L.; Alivisatos, A. P. *Nano Lett.* **2002**, *2*, 557−560.
(27) Miszta, K.; de Graaf, J.; Bertoni, G.; Dorfs, D.; Brescia, R.; Marras, S.; Ceseracciu, L.; Cingolani, R.; van Roij, R.; Dijkstra, M.; Manna, L. *Nat. Mater.* **2011**, *10*, 872−876.
(28) Wang, T.; Zhuang, J.; Lynch, J.; Chen, O.; Wang, Z.; Wang, X.; LaMontagne, D.; Wu, H.; Wang, Z.; Cao, Y. C. *Science* **2012**, *338*, 358−363.
(29) Paik, T.; Murray, C. B. *Nano Lett.* **2013**, *13*, 2952−2956.
(30) Liu, K.; Zhao, N.; Kumacheva, E. *Chem. Soc. Rev.* **2011**, *40*, 656−671.
(31) Li, M.; Schnablegger, H.; Mann, T. *Nature* **1999**, *402*, 393−395.
(32) Soulantica, K.; Maisonnat, A.; Fromen, M.-C.; Casanove, M.-J.; Chaudret, B. *Angew. Chem., Int. Ed.* **2003**, *42*, 1945−1949.
(33) Dumestre, F.; Chaudret, B.; Amiens, C.; Renaud, P.; Fejes, P. *Science* **2004**, *303*, 821−823.
(34) Desvaux, C.; Amiens, C.; Fejes, P.; Renaud, P.; Respaud, M.; Lecante, P.; Snoeck, E.; Chaudret, B. *Nat. Mater.* **2005**, *4*, 750−753.
(35) Lacroix, L.-M.; Lachaize, S.; Falqui, A.; Respaud, M.; Chaudret, B. *J. Am. Chem. Soc.* **2009**, *131*, 549−557.
(36) Warner, J. H.; Djouahra, S.; Tilley, R. R. *Nanotechnology* **2006**, *17*, 3035−3038.
(37) Cölfen, H.; Antonietti, M. *Mesocrystals and Nonclassical Crystallization*; John Wiley & Sons, Ltd: Chichester, U.K., 2008.
(38) Niederberger, M.; Cölfen, H. *Phys. Chem. Chem. Phys.* **2006**, *8*, 3271−3287.
(39) Fang, J.; Ding, B.; Gleiter, H. *Chem. Soc. Rev.* **2011**, *40*, 5347−5360.
(40) Abécassis, B.; Testard, F.; Spalla, O. *Phys. Rev. Lett.* **2008**, *100*, 115504.
(41) Loubat, A.; Impéror-Clerc, M.; Pansu, B.; Meneau, F.; Raquet, B.; Viau, G.; Lacroix, L.-M. *Langmuir* **2014**, *30*, 4005−4012.
(42) Cormary, B.; Dumestre, F.; Liakakos, N.; Soulantica, K.; Chaudret, B. *Dalton Trans.* **2013**, *42*, 12546−12553.
(43) Liakakos, N.; Cormary, B.; Li, X.; Lecante, P.; Respaud, M.; Maron, L.; Falqui, A.; Genovese, A.; Vendier, L.; Koïnis, S.; Chaudret, B.; Soulantica, K. *J. Am. Chem. Soc.* **2012**, *134*, 17922−17931.
(44) Nelson, R. C.; Miller, J. T. *Catal. Sci. Technol.* **2012**, *2*, 461−470.
(45) Krogman, J. P.; Gallagher, J. R.; Zhang, G.; Hock, A. S.; Miller, J. T.; Thomas, C. M. *Dalton Trans.* **2014**, *43*, 13852−13857.
(46) Panda, A.; Stender, M.; Olmstead, M. M.; Klavins, P.; Power, P. P. *Polyhedron* **2003**, *22*, 67−73.
(47) Murray, B. D.; Power, P. P. *Inorg. Chem.* **1984**, *23*, 4584−4588.
(48) Ellison, J. J.; Power, P. P.; Shoner, S. C. *J. Am. Chem. Soc.* **1989**, *111*, 8044−8046.
(49) Bartlett, R. A.; Power, P. P. *J. Am. Chem. Soc.* **1987**, *109*, 7563−7564.
(50) Sigel, G. A.; Bartlett, R. A.; Decker, D.; Olmstead, M. M.; Power, P. P. *Inorg. Chem.* **1987**, *26*, 1773−1780.
(51) Dehnen, S.; Zimmermann, C. *Eur. J. Inorg. Chem.* **2000**, *2000*, 1471−1473.
(52) Baisch, U.; Poli, R. *Polyhedron* **2008**, *27*, 2175−2185.
(53) Ward, A. J.; Masters, A. F.; Maschmeyer, T. In *Cobalt(II) Carboxylate Chemistry and Molecular Magnetism in Comprehensive Inorganic Chemistry II: From Elements to Applications*; Reedijk, J.; Poeppelmeier, K., Eds.; Elsevier: Oxford, U.K., 2013.
(54) Miller, J. T.; Kropf, A. J.; Zha, Y.; Regalbuto, J. R.; Delannoy, L.; Louis, C.; Bus, E.; van Bokhoven, J. A. *J. Catal.* **2006**, *240*, 222−234.
(55) De Yoreo, J. J.; Gilbert, P. U. P. A; Sommerdijk, N. A. J. M.; Penn, R. L.; Whitelam, S.; Joester, D.; Zhang, H.; Rimer, J. D.;

DOI: 10.1021/jacs.6b01929
J. Am. Chem. Soc. 2016, 138, 8422−8431

Navrotsky, A.; Banfield, J. F.; Wallace, A. F.; Michel, F. M.; Meldrum, F. C.; Cölfen, H.; Dove, P. M. *Science* **2015**, *349*, 6760 DOI: 10.1126/science.aaa6760.
(56) Finney, E. E.; Finke, R. G. *J. Colloid Interface Sci.* **2008**, *317*, 351−374.
(57) Park, S. Y.; Lytton-Jean, A. K.; Lee, B.; Weigand, S.; Schatz, G. C.; Mirkin, C. *Nature* **2008**, *451*, 553−556.
(58) Li, T.; Senesi, A. J.; Lee, B. *Chem. Rev.* **2016**, DOI: 10.1021/acs.chemrev.5b00690.
(59) Cui, H. G.; Pashuck, E. T.; Velichko, Y. S.; Weigand, S. J.; Cheetham, A. G.; Newcomb, C. J.; Stupp, S. I. *Science* **2010**, *327*, 555−559.
(60) Li, T.; Ye, B.; Niu, Z. W.; Thompson, P.; Seifert, S.; Lee, B.; Wang, Q. *Chem. Mater.* **2009**, *21*, 1046−1050.
(61) Li, T.; Zan, X.; Winans, R. E.; Wang, Q.; Lee, B. *Angew. Chem., Int. Ed.* **2013**, *52*, 6638−6642.
(62) Wu, H.; Yang, Y.; Cao, Y. C. *J. Am. Chem. Soc.* **2006**, *128*, 16522−16523.
(63) Baranov, D.; Fiore, A.; van Huis, M.; Giannini, C.; Falqui, A.; Lafont, U.; Zandbergen, H.; Zanella, M.; Cingolani, R.; Manna, L. *Nano Lett.* **2010**, *10*, 743−749.
(64) Lu, C.; Tang, Z. *Adv. Mater.* **2016**, *28*, 1096−1108.
(65) Huo, Z.; Tsung, C.-K.; Huang, W.; Zhang, X.; Yang, P. *Nano Lett.* **2008**, *8*, 2041−2044.
(66) Cölfen, H.; Mann, S. *Angew. Chem., Int. Ed.* **2003**, *42*, 2350−2365.
(67) Zhou, L.; O'Brian, P. O. *Small* **2008**, *4*, 1566−1574.
(68) Ma, M.-G.; Cölfen, H. *Curr. Opin. Colloid Interface Sci.* **2014**, *19*, 56−65.
(69) Bergstrôm, L.; Sturm, E. V.; Salazar-Alvarez, G.; Cölfen, H. *Acc. Chem. Res.* **2015**, *48*, 1391−1402.
(70) Cölfen, H.; Antonietti, M. *Angew. Chem., Int. Ed.* **2005**, *44*, 5576−5591.
(71) Song, R.-Q.; Cölfen, H. *Adv. Mater.* **2010**, *22*, 1301−1330.

DOI: 10.1021/jacs.6b01929
J. Am. Chem. Soc. 2016, 138, 8422−8431